Dalton Transactions

PAPER

Check for updates

Deciphering the mechanism of oxygen atom transfer by non-heme Mn[IV]−oxo species: an *ab initio* and DFT exploration†

Asmita Sen,‡[a] Nidhi Vyas, ID *‡[b] Bhawana Pandey[a] and Gopalan Rajaraman ID *[a]

Oxygen atom transfer (OAT) reactions employing transition metal–oxo species have tremendous significance in homogeneous catalysis for industrial use. Understanding the structural and mechanistic aspects of OAT reactions using high-valent metal–oxo species is of great importance to fine-tune their reactivity. Herein we examine the reactivity of a non-heme high-valent oxo-manganese(IV) complex, $[Mn^{IV}H_3buea(O)]^-$ towards a variety of substrates such as PPh_2Me, $PPhMe_2$, PCy_3, PPh_3, and PMe_3 using density functional theory as well as *ab initio* CASSCF/NEVPT2 methods. We have initially explored the structure and bonding of $[Mn^{IV}H_3buea(O)]^-$ and its congener $[Mn^{IV}H_3buea(S)]^-$. Our calculations affirm an $S = 3/2$ ground state of the catalyst with the $S = 5/2$ and $S = 1/2$ excited states predicted to be too high lying in energy to participate in the reaction mechanism. Our *ab initio* CASSCF/NEVPT2 calculations, however, reveal a strong multi-reference character for the ground $S = 3/2$ state with many low-lying quartets mixing significantly with the ground state. This opens up various reaction channels, and the admixed wave-function evolves during the reaction with the excited triplet dominating the ground state wave-function at the reactant complex. Our calculations predict the following pattern of reactivity, $PCy_3 < PMe_3 < PPh_3 < PPhMe_2 < PPh_2Me$ for the OAT reaction with the $Mn^{IV}\!\!=\!\!O$ species which correlates well with the experimental observations. Detailed electronic structure analysis of the transitions states reveal that these substrates react *via* an unusual low-energy δ-type pathway where a spin-up electron from the substrate is transferred to the $\delta^*_{x^2-y^2}$ orbital of the $Mn^{IV}\!\!=\!\!O$ facilitated by its multi-reference character. The unusual reactivity observed here has implications in understanding the reactivity of [Mn4Ca] species in photosystem II.

Introduction

There is considerable interest in the study of oxygen, sulphur and nitrogen atom transfer reactions in high-valent transition metal complexes, due to their vital role in many important biological enzymatic systems such as cytochrome P450, sulfite oxidase, phosphine oxides, nitrate reductase, dimethyl sulfoxide (DMSO) reductase and most importantly photosynthetic water oxidation in photosystem II.[1–9] In this direction, Mn–oxo complexes have been broadly explored and have proven to be very efficient. For instance, high-valent Mn–oxo species are involved in the oxidation of water by a tetra manganese cluster in the oxygen-evolving complex (OEC) in

photosystem II (PSII).[2,9,19] and also as an intermediate in certain catalases[20] and peroxidases.[21] Moreover, these high-valent metal oxo species have inspired a range of biomimetic studies, such as oxygen atom transfer and C–H bond activation reactions[7,10] and a detailed understanding of the mechanisms of these types of oxidative reactions will be helpful in the design of catalysts with increased efficiency and selectivity. Due to its biological and industrial ponderability, much attention has been paid to the study of oxygen atom transfer (OAT) reactions involving high-valent metal oxo complexes.[10–14] For these oxidative transformations, tertiary phosphines have become the reagents of choice, due to their high solubility in organic solvents and the ability to tune their reactivity through substitution at phosphorus.[11,14–18] Therefore, it is important to investigate the factors that control the reactivity of high-valent metal complexes with terminal oxo ligands. Based on the conclusions drawn from the above studies, several experimental groups have synthesised biomimetic models of these types of naturally occurring systems, which are also proposed to be competent oxidants in many organic transformations.

[a]*Department of Chemistry, Indian Institute of Technology Bombay, Mumbai 400076, India. E-mail: rajaraman@chem.iitb.ac.in*

[b]*School of Biotechnology, Jawaharlal Nehru University, New Delhi-110067, India*
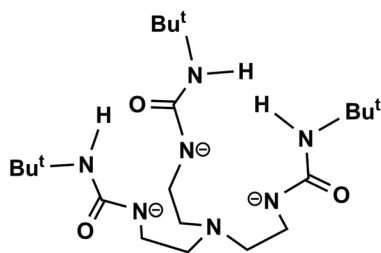
‡Both authors contributed equally.

Fig. 1 Chem-draw structure of the $[H_3buea]^{3-}$ ligand employed here.

Towards this direction, several experimental research groups have made considerable efforts in the generation and characterisation of high-valent manganese–oxo species.[12,13,22–27] For more than two decades Borovik and his group have been actively working on the development of non-heme Mn–oxo complexes with varying oxidation states of the metal, for instance, $[Mn^{III}H_3buea(O)]^{2-}$ and $[Mn^{IV}H_3buea(O)]^{-}$, and their related Mn-OH complexes, $[Mn^{II}H_3buea(OH)]^{2-}$ and $[Mn^{III}H_3buea(OH)]^{-}$ (where H_3buea is tris[(N′-tert-butylureaylato)-N-ethylene]aminato, see Fig. 1) and thoroughly characterised them using X-ray and spectroscopic methods.[14,28–33]

Computational studies have been proven to be extensively useful to gain insights into this area by exploring the structures, bonding and reactivity of the high-valent oxo species.[34–42] Recently, our group has elucidated the mechanism for the formation of the $Mn^{III}=O$ and $Mn^{IV}=O$ complexes starting from $[Mn^{II}H_2buea]^{2-}$ using molecular oxygen as the oxidant at room temperature.[36] Our group has also explored the mechanism of the hydrogen atom abstraction (HAT) reaction from DHA by $Mn^{III}=O$ and $Mn^{IV}=O$ complexes and examined the role of basicity in the reaction.[41] Borovik and co-workers also showed various sets of experiments that the $[Mn^{IV}H_3buea(O)]^{-}$ species perform very efficient OAT reactions while the corresponding $[Mn^{III}H_3buea(O)]^{2-}$ was unreactive.[14] Oxygen labelling studies further confirm that phosphine-oxide generated in the reactions are indeed from the oxygen atom of the $Mn^{IV}=O$ species. However, these OAT reactions are selective with some aryl phosphines readily yielding the corresponding phosphine-oxide while others do not. The mechanism of OAT reactions by $Mn^{IV}=O$ has not been well documented,[36,38,39] and there is a clear need to establish the factors which control the reactivity of the metal–oxo moieties towards oxygen transfer. This leads us to pursue a computational investigation for the formation of phosphine oxide using the $[Mn^{IV}H_3buea(O)]^{-}$ complex with various substrates. Furthermore, we have explored the isoelectronic $Mn^{IV}=S$ species and its ability to perform sulphur atom transfer (SAT) reactions. There is a vast body of literature documenting SAT reactions with various catalysts, including some dinuclear Mn systems,[43–45] however there is no report on high-valent $Mn^{IV}=S$ species while the high-valent analogues of Fe are well characterised.[46]

In this manuscript, we have studied the intricate mechanistic details of oxygen atom transfer reactions using the $[Mn^{IV}H_3buea(O)]^{-}$ complex with a variety of substrates such as; PPh_2Me, $PPhMe_2$, PCy_3, PPh_3, and PMe_3 forming phosphine oxides. By probing the structure and bonding properties of the $Mn^{IV}=O$ species and the corresponding transition states, we would like to comment on the reactivity of high-valent manganese–oxo species. In addition, we have investigated computationally a relatively unexplored sulphur atom transfer reaction (SAT) by $Mn^{IV}=S$ species. In this work, we aim to address the following questions using a combination of DFT and *ab initio* CASSCF/NEVPT2 method (i) what is the ground state electronic structure of the $Mn^{IV}=O$ and $Mn^{IV}=S$ species, and how do they differ? (ii) What is the exact mechanism by which the OAT reaction takes place and why do the $Mn^{IV}=O$ species exhibit differential oxidative abilities with substrates such as PCy_3, PPh_3, PPh_2Me, $PPhMe_2$ and PMe_3? (iii) How do SAT and OAT reactions differ and is SAT reaction with $[Mn^{IV}H_3buea(S)]^{-}$ species feasible with PR_3 substrates?

Computational methods

Density functional theory (DFT) calculations were carried out using the Gaussian 09 suite of programs.[47,48] Geometries of all global minima and the transition state in the gas phase were optimised without any symmetry constraints using the unrestricted B3LYP hybrid functional[49–51] as this hybrid density functional has been proven to provide an accurate description of structure and energies for such reactions.[36,39] Moreover, earlier benchmarking performed by us also indicates the superiority of this functional for predicting correct spin-state ordering, spectroscopic parameters and reactivity trend.[41] Two different basis sets were used; LanL2DZ encompasses a double-ζ quality basis set with the Los Alamos effective core potential for $Mn^{52,53}$ and a 6-31G** basis set for the other atoms such as C, H, N, O, P and S.[54] Refinement of the electronic energies have been performed *via* single-point calculations on the optimised geometries using the TZVP basis set for all atoms at the same level of theory. The harmonic vibrational frequency calculations were performed to characterise all the stationary points at the temperature of 298.15 K. Both the global minima and the maxima in the potential energy surface were verified by visualising the vibrational modes where all the minimum energy structures are characterised by all positive frequencies. In contrast, the transition states were characterised by a single negative frequency. Intrinsic reaction coordinate (IRC) calculations were carried out to confirm the fact that, all the calculated transition states are connecting to the corresponding intermediates. The role of solvent on the gas phase energetics was studied at the B3LYP level using Solvation Model Based on Density (SMD).[55] Here dimethyl sulfoxide (DMSO) is used as a solvent. Grimme's D3 version of dispersion with the original D3 dumping function has been incorporated *via* the DFT-D3 method in the gas phase optimisation as well as in the single-point calculations.[56,57] The quoted DFT energies are B3LYP-D3 electronic energies, including zero-point energy corrections, which

were obtained from the frequency calculations. NBO analysis was performed using the G09 suite to calculate the Wiberg bond order.[58] Calculations of spectroscopic properties such as UV-VIS spectra and EPR parameters were performed using the ORCA 3.0.1 program package.[59] For these calculations, relativistic effects were taken into account *via* zeroth-order regular approximation (ZORA),[60,61] which was used both in the Hamiltonian as well as in basis functions. In the configuration interaction (CI) step,[62] state-averaged complete-active space self-consistent field (CASSCF) wave functions have been employed with the 10-quartet and 40-doublets considering three active metal electrons in five metal d-orbitals using the def2-TZVP basis set on Mn, def2-TZVP(-f) basis set for N and def2-SVP basis set on C, O, S and H. Further to incorporate dynamic correlation, N-electron valence perturbation theory (NEVPT2) was performed on top of the CASSCF wave-function. Increased integration grids (Grid 5 in ORCA convention) along with tight SCF convergence were used. The hybrid B3LYP functional has been used for both TD-DFT and CASSCF/NEV calculations.

In this study, the complete active space self-consistent-field (CASSCF) method has been used to expand the electronic wave-function in all possible configuration state functions by the distribution of electrons in the active space. Although computationally costly, this method is more simplified and accurate than the DFT method to determine both the ground state and the excited state wave-functions by state-specific configuration interaction (CI).[73] It is important to note here that when the mixing of the wave function is significant as seen in the performed CASSCF calculations, DFT calculations may not yield accurate results. However, to compensate this factor, we have explored various reaction channels σ, π, and δ which indirectly captures the multi-reference character observed in CASSCF calculations to some extent. In general, the DLPNO-CCSD(T) methods proposed recently for the estimation of spin-state energies offer a viable alternative to DFT methods.[74] However, this method may not yield a good numerical estimate of energies in the present case, given the strong multi-reference character of the Mn^{IV}=O species (*vide infra*).

To understand the origin of kinetic barrier heights observed with different substrates, we have performed the energy decomposition analysis (EDA) using AOMIX software.[63] The spin-density plots were generated using Chemcraft version 1.6.[64] In this study, we have calculated the rate constant of these oxygen transfer reactions following the Eyring equation depicted by eqn (1), where $\Delta G^{\ddagger}$ is the activation free energy, κ is the transmission coefficient (which can be treated as a unit for the sake of simplicity).

$$k = \kappa \frac{k_B T}{h} e^{-\frac{\Delta G^{\ddagger}}{RT}} \qquad (1)$$

We have computed Wiberg bond indices from the natural atomic orbital analysis (NBO) and bond formation index (BF$_i$) or bond cleavage index (BC$_j$) have been calculated from the calculated bond orders, following the equation described below,

$$BF_i \text{ or } BC_j = \frac{BO_i^{TS} - BO_i^R}{BO_i^P - BO_i^R} \times 100$$

From the above calculated BF$_i$ and BC$_j$ values, Bond formation-cleavage average (BFC$_{Ave}$) values have been calculated as,[69]

$$BFC_{Ave} = 1/2(BF_i + BC_f)$$

Here, we have used notations for easy understanding of the various spin states, for instance, $^{2S+1}$[species name]$_{x(\delta/\sigma)}$, where, S is the spin state of the metal, and x denotes the number representing the substrates such as 1 for PPh$_2$Me, 2 for PPhMe$_2$, 3 for PPh$_3$, 4 for PCy$_3$ and 5 for PMe$_3$. The notation $^{2S+1}$[species name]$_S$ has been used for all reactions. If two types of pathways are involved, this is represented by (δ) or (σ) after the substrate notation in the subscript. Also, to reduce the computational cost and time, we have replaced the terminal tertiary-butyl groups of the [H$_3$buea] ligand by the methyl group.

Results and discussion

In the first section, electronic structure, bonding and computed EPR parameters for the [Mn^{IV}H$_3$buea(O)]$^-$ and [Mn^{IV}H$_3$buea(S)]$^-$ species will be discussed followed by the mechanism of OAT reaction by this species in the next section.

Electronic structure of [Mn^{IV}H$_3$buea(X)]$^-$ (X=O and S) species

We have optimised [Mn^{IV}H$_3$buea(O)]$^-$ species in all possible spin states *i.e.* S = 3/2 and S = 1/2. In addition, we have also computed the energy of Mn^{III}–O$^{\bullet}$ form where we performed calculations on an S = 5/2 state which corresponds to a Mn^{III} centre ferromagnetically coupled with the oxyl radical centre. While there is a possibility of obtaining an S = 3/2 state when there is antiferromagnetic interaction between the Mn^{III} centre and the oxyl radical, all our attempts to obtain such species converged to the S = 3/2 Mn^{IV}=O species with no concomitant negative spin density at the oxygen atom as expected. This suggests that such a configuration is unlikely to be stable as there is a global minima for the S = 3/2 state.[35] In recent reports on the reactivity of Mn^{IV}=O species, the reactivity was suggested to be generated from the excited S = 3/2 state instead of the ground state.[34,35] We have also computed this excited state to obtain a good numerical estimate of the barrier heights for the OAT reaction. DFT calculations predict the S = 3/2 state as the ground state with the high-spin S = 5/2 and low-spin S = 1/2 states lying 70.4 kJ mol^{-1} and 98.8 kJ mol^{-1} higher in energy, respectively (see Fig. 2). The optimised structure for the ground S = 3/2 state along with the respective spin density plots are shown in Fig. 3a and b. In the S = 3/2 state, the Mn–O bond distance is computed to be 1.68 Å (see Fig. 3a). Unlike the popular Fe^{IV}=O species for which detail structural information is available, there are only scarce

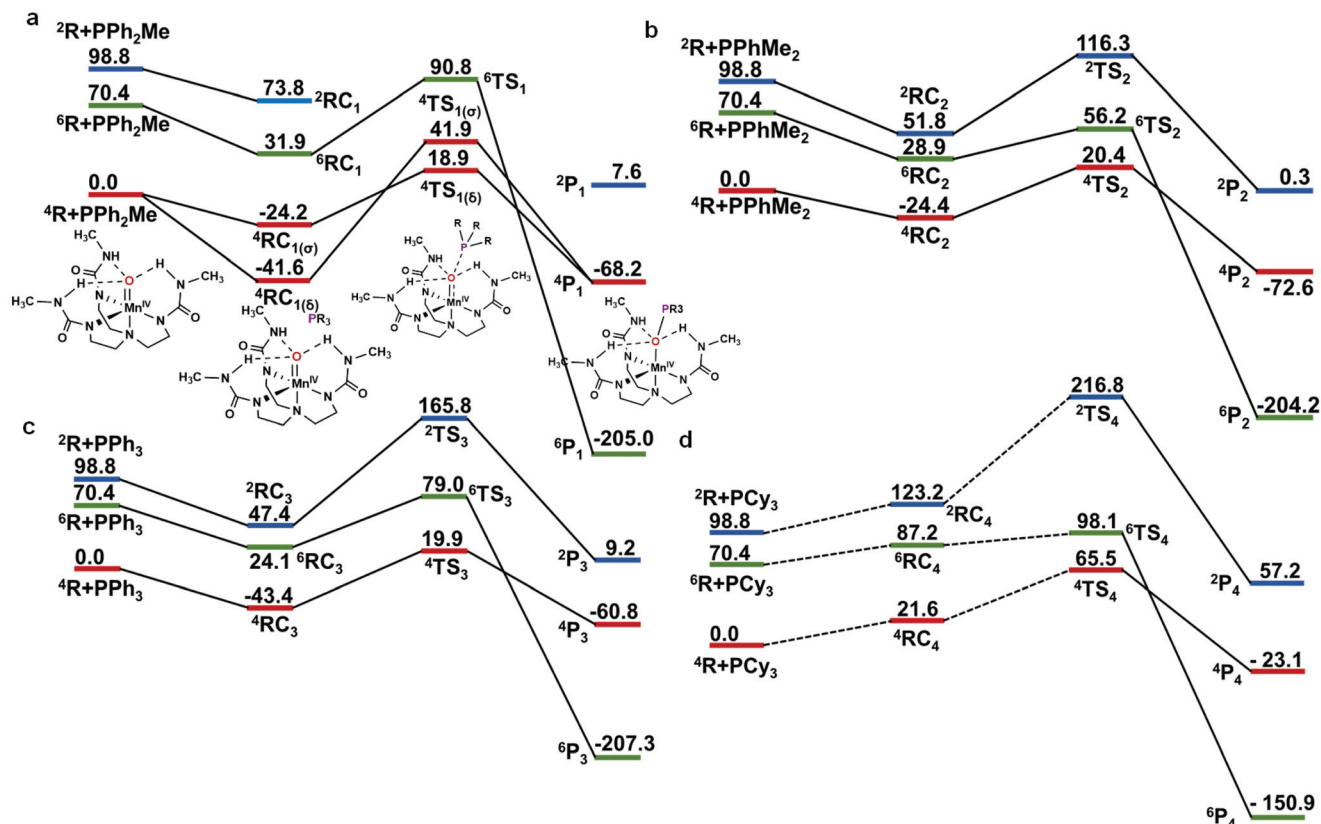**Fig. 2** DFT/B3LYP-D3 computed energy profile diagram (kJ mol^{-1}) of the oxygen atom transfer reactions for (a) PPh$_2$Me, (b) PPhMe$_2$, (c) PPh$_3$, and (d) PCy$_3$ using the [Mn^{IV}H$_3$buea(O)]$^-$ catalyst.
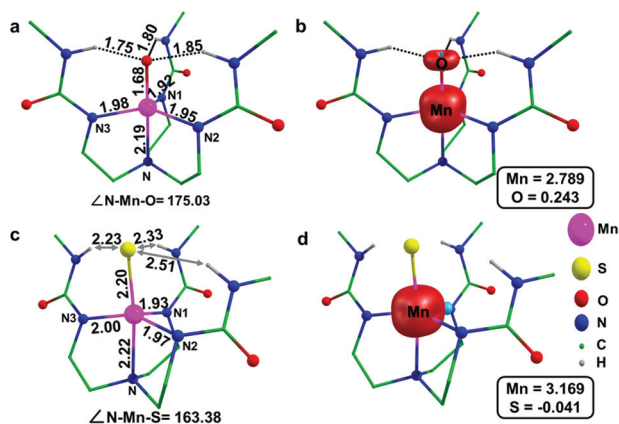

Fig. 3 DFT optimized structures and spin density plots of (a and b) the [Mn^{IV}H$_3$buea(O)]$^-$ complex in the S = 3/2 ground state, (c and d) the [Mn^{IV}H$_3$buea(S)]$^-$ complex in the S = 3/2 ground state.

reports on the geometry of the analogues Mn^{IV}=O species. So far there is only one report on the X-ray structure of Mn^{IV}=O species, [Mn^{IV}(O)(ditox)$_3$]$^-$ (where Hditox = ^{t}Bu$_2$MeCOH), with the Mn^{IV}=O centre being four coordinate in a pseudo-tetrahedral C_{3v} geometry with the Mn–O distance reported to be 1.628 Å possessing S = 3/2 ground state affirmed by SQUID and EPR data.[65] In addition, a series of six-coordinate Mn^{IV}=O

species has been characterised using XAFS study revealing the Mn–O distance in the range of 1.68 to 1.78 Å.[12,66] This distance is also consistent with EXAFS data reported for the square pyramidal five-coordinate [Mn^{IV}(O)(Tpiv)] species (here Tpiv = *meso*-tetrakis(α,α,α,α-*o*-pivalamidephenyl)porphyrin).[12,67] The Mn–O bond in the S = 3/2 state is 0.05 Å shorter than the Mn^{III}-O$^•$ species (S = 5/2) indicating a stronger Mn–O double bond character for this species in the S = 3/2 state (see Table S1 of the ESI† for geometrical parameters). This fact is also supported by the Wiberg bond index of 1.573 (see Table 1). Furthermore, the oxo centre of the Mn–O moiety makes a hydrogen bonding cavity of ∼1.80 Å radius interacting with the dangling hydrogen atoms from the nitrogen sites of the buea-ligand. This bond is weaker than the Mn^{III}–O$^•$ species, where the radius is ∼1.74 Å. The other optimised parameters, for instance, N1–Mn–N2, N2–Mn–N3 and N3–Mn–N1, N–Mn–O angles are computed to be 103.1°, 137.9°, 112.3°, 175.0° respectively. These angles suggest a strong deviation from the trigonal symmetry. This distortion in the trigonal plane is expected as the Mn^{IV} system having a d^3 configuration with trigonal bipyramidal geometry is Jahn–Teller active and expected to undergo structural distortion. Spin density on the Mn atom is found to be 2.789 along with a significant spin density of 0.243 on the oxygen atom (see Fig. 3b and Table S2 of the ESI†).

Table 1 Computed NBO, EDA (in kJ mol^{-1}), WB index and ZFS values for the [Mn^{IV}H$_3$buea(O)]$^-$ and [Mn^{IV}H$_3$buea(S)]$^-$ species

Species	NBO		EDA			WB index	EPR	
			H$_3$buea(Mn) + O(S)					
	Metal (%)	O (%)	ΔE_{int}	ΔE_{steric}	ΔE_{orb}		D (cm^{-1})	E/D
Mn^{IV}=O	23.65	76.35	−2713.7	982.4	−731.3	1.573	4.01	0.26
Mn^{IV}=S	30.02	69.98	−1731.3	802.1	−929.3	1.556	3.05	0.22

The DFT computed ground-state electron occupancy for the Mn^{IV}=O species in the d-block orbitals is $\delta_{xy}^{1}\pi^{*}_{yz}^{1}\pi^{*}_{xz}^{1}\delta^{*}_{x^2-y^2}^{0}\sigma^{*}_{z^2}^{0}$, as depicted in Fig. 4a. The degeneracy of the two π orbitals (π^{*}_{xz} and π^{*}_{yz}) is lifted, and these are destabilised by 0.2 eV and 0.5 eV, respectively from the lowest-lying δ_{xy} orbital. The empty $\delta^{*}_{x^2-y^2}$ and $\sigma^{*}_{z^2}$ orbitals are found to be very high in energy lying at 3.4 eV and 5.1 eV compared to the lowest δ_{xy} orbital. The UV-VIS absorption spectrum for the [Mn^{IV}H$_3$buea(O)]$^-$ catalyst computed from TD-DFT analysis consists of low energy weak bands at 930 nm (band *a*) and 779 nm (band *b*), an intense band at 596 nm (band *c*), a high energy sharp band at 404 nm (band *d*) and higher energy features above 400 nm (see Fig. S1 in the ESI†). Here the feature noted as band *a* in the near-IR region (930 nm) corresponds to the transition from $^4E \rightarrow {}^4B$ (from $\pi^{*}_{xz}/\pi^{*}_{yz}$ to $\delta^{*}_{x^2-y^2}$ orbital) and this is in agreement with earlier experiments[34] reporting such unique features for Mn^{IV}=O species. The TD-DFT computed sharp band at 596 nm is in accordance with the experimental absorption at 635 nm.[14] The band *c* also corresponds to d–d transition while band *d* belongs to LMCT transitions (see Fig. S1†).

Similar to the band *d*, the high energy bands also originate due to the strong ligand to metal charge transfer.

To further understand the underlying electronic structure of the ground state *S* = 3/2 geometry, state-average CASSSF/NEVPT2 calculations were performed on the *S* = 3/2 ground state geometry. Here we have included ten quartet and 40 doublet states. Calculations reveal a strong mixing of the ground state electronic structure. Particularly, the dominant ground state electronic structure ^4B is found to have $\delta_{xy}^{1}\pi^{*}_{yz}^{1}\pi^{*}_{xz}^{1}\delta^{*}_{x^2-y^2}^{0}\sigma^{*}_{z^2}^{0}$ configuration with mere 32% contribution and is found to mix strongly with ^4E states with $\delta_{xy}^{1}\pi^{*}_{yz}^{0}\pi^{*}_{xz}^{1}\delta^{*}_{x^2-y^2}^{1}\sigma^{*}_{z^2}^{0}$ and $\delta_{xy}^{1}\pi^{*}_{yz}^{1}\pi^{*}_{xz}^{0}\delta^{*}_{x^2-y^2}^{0}\sigma^{*}_{z^2}^{1}$ excited states contributing 18% and 17%, respectively to the ground state (see Fig. 4b and Table S3†). Such strong mixing reveals the multiconfigurational character of the Mn^{IV}=O species and such complex electronic features are unlikely to be captured by single determinant methods such as DFT. To assess the utilisation of the CASSCF/NEVPT2 method to obtain a detailed electronic structure, we have calculated zero-field splitting parameters for [Mn^{IV}H$_3$buea(O)]$^-$ species using the CASSCF/
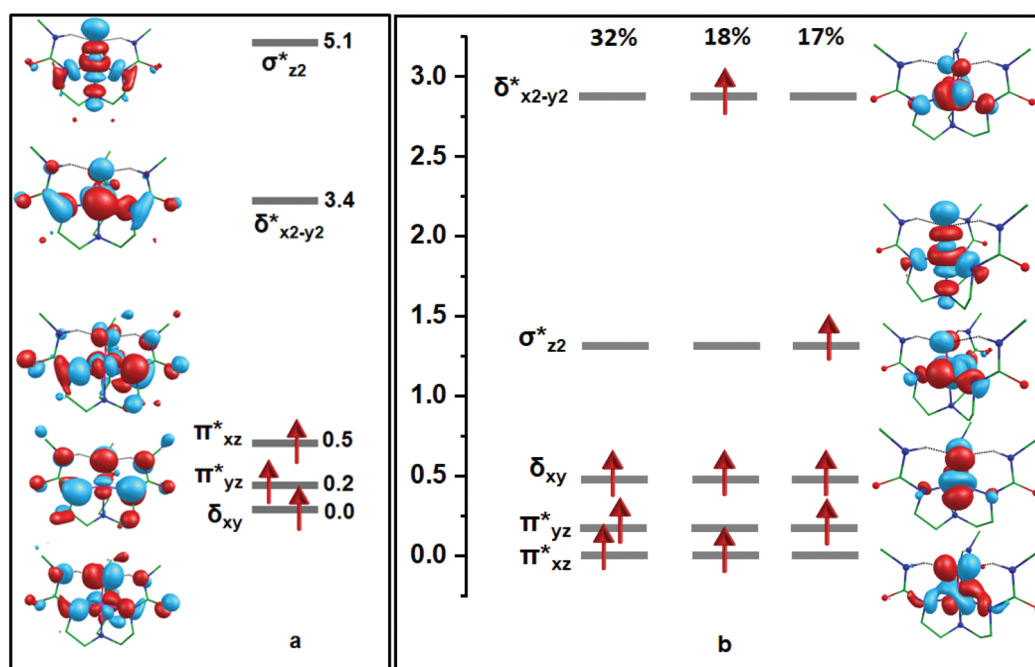

Fig. 4 (a) DFT computed and (b) CASSSFT/NEVPT2 based frontier d-based orbital energies of the *S* = 3/2 state for [Mn^{IV}H$_3$buea(O)]$^-$ species. All the energy values are in eV unit.

NEVPT2 method. The D and E/D values are found to be 4.01 cm^{-1} and 0.26, which fits well with the experimental estimate of $D \sim 3.0$ cm^{-1} and $E/D = 0.26$.[14] Here both the magnitude, as well as the sign of D, are reproduced. The calculations estimate a strong, easy plane anisotropy arising perhaps due to the splitting of the π^*_{xz} and π^*_{yz} orbitals. A significant contribution to the ZFS parameter D arises from π^*_{yz} to $\sigma^*_{z^2}$ (-0.412 cm^{-1}) and π^*_{yz}/π^*_{xz} to the $\delta^*_{x^2-y^2}/\sigma^*_{z^2}$ ($+0.919$ cm^{-1}) quartet states. Much larger and dominant positive contributions are found to arise from spin–flip doublet states aided by the strong mixing of the wave function at the ground state. Particularly doublet transition from δ_{xy} to $\delta^*_{x^2-y^2}$ orbitals contributing $+1.80$ cm^{-1} and π^*_{xz} to $\sigma^*_{z^2}$ contributes $+2.45$ cm^{-1} to the overall D value. The electronic g-tensors for the $S = 3/2$ state is calculated to be $g_x = 1.623$, $g_y = 2.357$ and $g_z = 5.116$. This reveals a rhombic pattern of g-tensors, and this is also consistent with experimental reports.[14,24,68]

Although synthesis and characterisation of $[Mn^{IV}H_3buea(S)]^-$ species is not reported, analogues of $[Fe^{III}H_3buea(S)]^-$ species have been reported earlier.[46] This prompts us to look into the congener of the oxo analogue and the relevant sulphur atom transfer reactions. The $[Mn^{IV}H_3buea(S)]^-$ species also possess an $S = 3/2$ ground state with the $S = 5/2$ and $S = 1/2$ lying at 8.6 kJ mol^{-1} and 113.9 kJ mol^{-1} higher in energy (see Fig. 5). A significant difference in the sextet/quartet energy gap for oxo (70.2/0.0) and sulphido (8.6/0.0) species suggests that the spin state energetics are greatly affected by the substitution. Particularly the $S = 5/2$ state is very close to the $S = 3/2$ state, suggesting a strong contribution of Mn^{III}–S$^{\cdot}$ to the ground Mn^{IV}=S species. This also indicates that increasing the covalency of the donor atom is likely to stabilise the higher oxidation state at the metal due to enhanced electron donation. The computed Mn–S bond length for this complex on the $S = 3/2$ state is estimated to be 2.20 Å (see Fig. 3c), which is 0.52 Å longer than that of Mn^{IV}=O species on the same surface. A slightly higher value of the WB index for Mn–O (1.573) than that of the Mn–S (1.556) reflects a higher double bond character in the Mn–O bond. The computed spin density on the Mn atom in Mn^{IV}=S is observed to be 3.170, and this is significantly larger than that found at the Mn centre of the Mn^{IV}=O species in the ground $S = 3/2$ state. This increase in spin density at the Mn centre is accompanied by a drastic reduction of spin density at the sulphur centre (-0.041) suggesting the absence of radical character at the S atom (see Fig. 3d). Further NBO analysis reveals that the σ-bonding interaction in the Mn^{IV}=O species is composed of 23.65% of Mn-d_{z^2} and 76.35% of O(P_z) orbitals while that for the Mn^{IV}=S species is 30.02% of Mn-d_{z^2} and 69.98% of S(P_z) orbitals (Table 1). These contributions suggest the greater covalent nature of the Mn-S bond than that of the Mn-O. We have further calculated the zero-field splitting parameters for the $[Mn^{IV}H_3buea(S)]^-$ species at the $S = 3/2$ state and the values are found to be $D = 3.05$ cm^{-1} and $E/D = 0.22$. The electronic g-tensors for the ground state of the Mn^{IV}–S complex are estimated to be $g_x = 1.716$, $g_y = 2.589$ and $g_z = 5.033$, indicating a rhombic pattern of g-tensor similar to the Mn^{IV}–O species. Further EDA analysis performed (see Table 1) revealed that the Mn^{IV}=O bond is nearly 1.56 times stronger than the Mn^{IV}=S bond and this stabilisation essentially arises from significant orbital stabilisation energy as oxygen 2p orbitals overlap very efficiently with the metal orbitals than the sulphur 3p orbitals.

Mechanism of oxygen atom transfer reactions

Experimentally, it is found that $[Mn^{IV}H_3buea(O)]^-$ species do not react with substrates such as PCy$_3$ and PPh$_3$ at room temperature in DMSO solvent. In contrast, it reacts with PPh$_2$Me
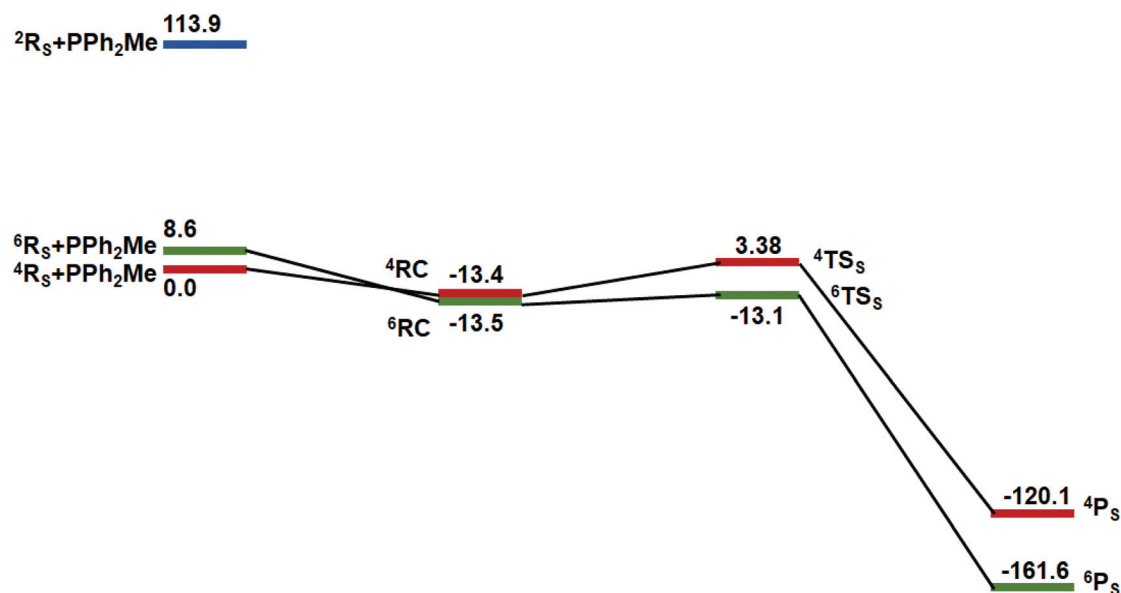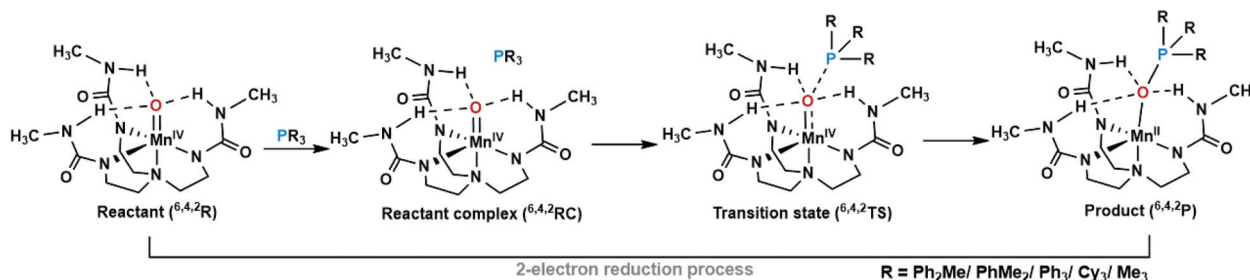
Fig. 5 DFT/B3LYP-D3 computed energy profile diagram (kJ mol^{-1}) for the S-atom transfer reactions for the substrate PPh$_2$Me with $[Mn^{IV}H_3buea(S)]^-$ species.

Scheme 1 Schematic diagram from the oxygen atom transfer reaction.

and PPhMe$_2$ substrates producing corresponding phosphine oxides and the reduced form of the catalyst, [Mn^{II}H$_3$buea]$^-$, *via* a two-electron transfer process under the same reaction conditions.[14] The average yield for the reaction with PPh$_2$Me is 50–70% while that of PPhMe$_2$ is ~50%. Oxygen atom transfer reactions to the phosphine complexes with other metal–oxo species employ PMe$_3$ as a substrate;[17] thus we have considered all five substrates to understand the electronic as well as structural reasons behind their reactivity pattern. The schematic mechanism adapted for the oxygen atom transfer reaction is shown in Scheme 1. The overall reaction comprises of initial reactant complex formation, ^{6,4,2}RC, between the free catalyst and the phosphine substrates, followed by simultaneous bond breaking (π bond of Mn^{IV}=O) and bond formation (O···PR$_3$) events involved in the synchronous oxygen-transfer transition state (^{6,4,2}TS) and eventually leads to the formation of the Mn^{II}-phosphine oxide product complex, [Mn^{II}H$_3$buea(OPR$_3$)]$^-$ (^{6,4,2}P). In the next section, we will thoroughly discuss the mechanistic and structural aspects of the individual substrates. The DFT computed potential energy diagrams for the PPh$_2$Me, PPhMe$_2$, PPh$_3$ and PCy$_3$ substrates are given in Fig. 2.

Starting from the PPh$_2$Me substrate and the free catalyst [Mn^{IV}H$_3$buea(O)]$^-$, interestingly, we have found two reactant complexes with varying intermediate spin configurations, ^{4}RC$_{1(\sigma)}$ which is exergonic by 24.2 kJ mol^{-1} having the electronic configuration of $\sigma*_{z^2}{}^1\delta_{xy}{}^1\delta*_{x^2-y^2}{}^0\pi*_{yz}{}^1\pi*_{xz}{}^0$ (see Table S4†) and the other one ^{4}RC$_{1(\delta)}$ with the $\delta*_{x^2-y^2}{}^1\pi*_{yz}{}^1\pi*_{xz}{}^1\delta_{xy}{}^0\sigma*_{z^2}{}^0$ configuration (see Table S5 in the ESI†) is 41.6 kJ mol^{-1} exothermic.

To understand the multiconfigurational character of the reactant complex, CASSCF calculations were performed on both geometries. The calculations reveal a strong multi-determinant characteristic of ground state $S = 3/2$ (see Table S3 in the ESI†) at the *RC* with the ground state electronic configuration $\delta_{xy}{}^1\pi*_{yz}{}^1\pi*_{xz}{}^1\delta*_{x^2-y^2}{}^0\sigma*_{z^2}{}^0$ contributing less than 6% with $\delta_{xy}{}^1\pi*_{yz}{}^1\pi*_{xz}{}^0\delta*_{x^2-y^2}{}^0\sigma*_{z^2}{}^1$ dominating the ground state wavefunction (38%) for the ^{4}RC$_{1(\sigma)}$ species. This suggests that as we move along the reaction coordinate, the composition of the ground state electronic structure predicted changes, with the electronic configuration contributing 17% to the ground state for the free catalyst becoming dominant at the reactant complex stage as this configuration is driving the reactivity further yielding a lower energy transition state.

It is important to compare our results to the earlier results reported by Jackson and co-workers on [Mn^{IV}(O)(N4Py)]$^{2+}$ species using CASSCF/NEVPT2 methods.[34] As this is an octahedral Mn^{IV}=O species, clearly the orbital ordering is different compared to ours. Further on the $\delta*_{x^2-y^2}$ orbital did not have any contribution from the oxygen atom and therefore the δ pathway is unlikely in this case, and the lowest barriers are estimated on the σ channels. In addition, CASSCF/NEVPT2 analysis reveals that the ground state has dominant $\delta_{xy}{}^1\pi*_{yz}{}^1\pi*_{xz}{}^1\delta*_{x^2-y^2}{}^0\sigma*_{z^2}{}^0$ character (77%) with little mixing seen with other quartets, however, a small (6%) but important Mn^{III}–O$^•$ mixing has been unveiled. This is very different from our results with strong mixing with other quartet states has been witnessed suggesting diverging reactivity for the TBP–Mn^{IV}=O compared to octahedral-Mn^{IV}=O species. This kind of behaviour was reported earlier for Fe^{IV}=O species wherein TBP-Fe^{IV}=O was found to be aggressive in its reactivity compared to octahedral Fe^{IV}=O species.[71]

The energy barrier for the oxygen atom transfer is estimated to be 43.1 kJ mol^{-1} (^{4}RC$_{1(\sigma)} \rightarrow {}^4TS_{1(\delta)}$) in the quartet ($S = 3/2$) energy surface (see Fig. 2a). The energy barrier associated with the ^{4}RC$_{1(\delta)}$ is quite high, 83.5 kJ mol^{-1}. Therefore, the pathway associated with the higher energy barrier can be eliminated from our calculations. Other spin states such as $S = 5/2$ and $S = 1/2$ are lying at 56.1 kJ mol^{-1} and 98.0 kJ mol^{-1} higher in energy than that of ^{4}RC$_{1(\sigma)}$ (see Fig. 2a). Therefore, we can easily discard the possibility of these two spin-surfaces too from taking part in the reaction kinetics for PPh$_2$Me. The Mn–O bond distance (1.67 Å) is not altered much in the ^{4}RC$_{1(\sigma)}$ as compared to the bare catalyst (^{4}R). However, the hydrogen-bonding cavity is distorted in one side (2.05 Å) in the reactant complex to allow the substrate to approach oxygen closely at the transition state. In ^{4}TS$_{1(\delta)}$, the Mn–O bond is elongated to 1.72 Å which is comparable with the Mn^{III}=O bond length (1.73 Å) (longer than the Mn^{IV}–O double bond but shorter than that of Mn^{II}–O$^•$ single bond).[36,42] The limiting P···O distance in ^{4}TS$_{1(\delta)}$ is found to be 2.33 Å which is much longer than the regular P–O single bond length (see Fig. 6a and Table S1 in the ESI†). The above bonding parameters are indicative of the fact that in the transition state, neither the Mn–O double bond is breaking completely nor the P–O bond is fully forming, but a synchronous type of oxo-transfer is taking place. This low-lying transition state follows the
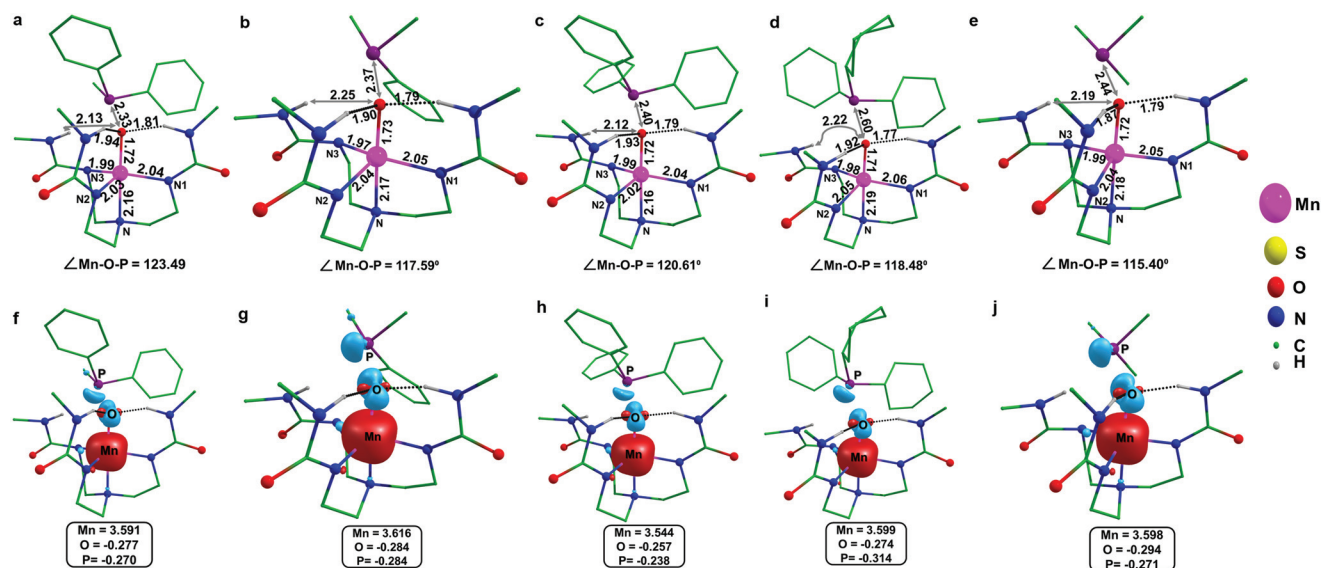
Fig. 6 DFT/B3LYP-D3 optimised structures of (a) $^4TS_{1(\delta)}$, (b) $^4TS_2$, (c) $^4TS_3$, (d) $^4TS_4$, (e) $^4TS_5$, and respective spin densities of (f) $^4TS_{1(\delta)}$, (g) $^4TS_2$, (h) $^4TS_3$, (i) $^4TS_4$, (j) $^4TS_5$.

δ-pathway, where the Mn–O–P angle is estimated to be 123.49°. In $^4TS_{1(\delta)}$, the spin density on the Mn centre is found to be 3.591 with the O and P centre possessing a spin density of −0.277 and −0.270 (see Fig. 6a and f). A significant increase in the spin density of 0.762 on the Mn centre and negative residual spin densities on the O and P centres indicate the transfer of α-electron from the respective 3S and 2P orbitals of the P and O centres to the metal $\delta^*_{x^2-y^2}$ orbital. The higher energy $^4TS_{1(\sigma)}$ is 23.0 kJ mol^{-1} uphill compared to that of $^4TS_{1(\delta)}$ (see Fig. 2a and Fig. S2†). Fig. 7a depicts that there are three-unpaired spin-up electrons in the π^*_{yz}, δ_{xy} and $\sigma^*_{z^2}$ orbitals and with the occupancy of 0.23 and 0.14 in $\delta^*_{x^2-y^2}$ and π^*_{xz} orbitals, respectively in $^4RC_{1(\sigma)}$. As argued before, after electron transfer in the $^4TS_{1(\delta)}$ state, the d-block of the metal gains an electron into the partially vacant $\delta^*_{x^2-y^2}$ orbital of the metal while the 2p of O and 3S orbital P is left with a significant amount of spin-down electrons (see Fig. 7b).[25,35] The spin density of 3.567, −0.207, −0.287 on the metal, O and the P centres and the Mn–O–P bond angle of 158.3° in this high-lying transition state is indicative of the transfer of α-electron to the metal vacant $\sigma^*_{z^2}$ orbital in a similar fashion (see Fig. 7c and d). This alternative high energy transition state is associated with the σ-pathway and designated as $^4TS_{1(\sigma)}$. Due to transfer of α-spin to the metal d-orbital from the O and P centres in both the transitions states, the increase of the exchange term (K_{dd}) will be equal ($3K_{dd}$) in both cases (see Fig. 8). Therefore, the stability of the $^4TS_{1(\delta)}$ over $^4TS_{1(\sigma)}$ is not due to the exchange enhance reactivity (EER)[42] but orbital dependent.

Our results from the DFT along with *ab initio* CASSCF/ NEVPT2 calculations are consistent with the observations depicted by Shaik and co-workers while studying the C–H bond activation catalysed by a non-heme Mn^{IV}=O species.[35] They have also pointed toward the interplay of the two S = 3/2

states for the reactivity of the Mn^{IV}=O species and the involvement of higher energy S = 3/2 configuration to the catalytic reactivity. Although the Mn^{IV}=O complexes in the heme environment may not involve these higher energy states in their reactivity.[72]

After the oxo-transfer, the product formation takes place where a spin-crossover between the S = 5/2 and S = 3/2 states is expected to occur. The formation of the product is highly exothermic from the free catalyst as well for the reactant complex and lies 180.8 kJ mol^{-1} downhill compared to that of the reactant complex on the S = 3/2 surface. In $^6P_1$, the Mn–O bond further elongates to 2.25 Å, and P–O bond is fully formed (1.51 Å). We have calculated the rate of this oxo-transfer reaction for the substrate PPh$_2$Me using Eyring equation and the DFT estimated rate is 1.7 × 10^5 M^{-1} s^{-1}. This very high rate coincides with the experimental observation, and we can conclude that PPh$_2$Me reacts very fast with the Mn^{IV}=O catalyst towards the formation of phosphine oxide.

Similar to the PPh$_2$Me, the reactant cluster formation for PPhMe$_2$ is also exothermic by 24.4 kJ mol^{-1} from the free catalyst in the ground S = 3/2 state ($^4RC_2$). The other two spin states are lying 53.3 kJ mol^{-1} (S = 5/2) and 76.2 kJ mol^{-1} (S = 1/2) higher in energy (see Fig. 2b). From these energy values, we can ignore the participation of the higher energy doublet state. The lowest energy barrier for the oxygen atom transfer ($^4RC_2 \rightarrow ^4TS_2$) in the present case is associated with 44.8 kJ mol^{-1} in the quartet (S = 3/2) energy surface (see Fig. 2b). Therefore, we can conclude that the reaction is occurring in the S = 3/2 surface only. The barrier height computed here is roughly 1.7 kJ mol^{-1} higher than the PPh$_2$Me substrate. The calculated rate of the oxo-transfer reaction for the substrate PPhMe$_2$ is estimated to be 8.5 × 10^4 M^{-1} s^{-1}, which is nearly two times lower than the rate of PPh$_2$Me. This slightly higher barrier compared for the PPh$_2$Me is also in line with the experimental
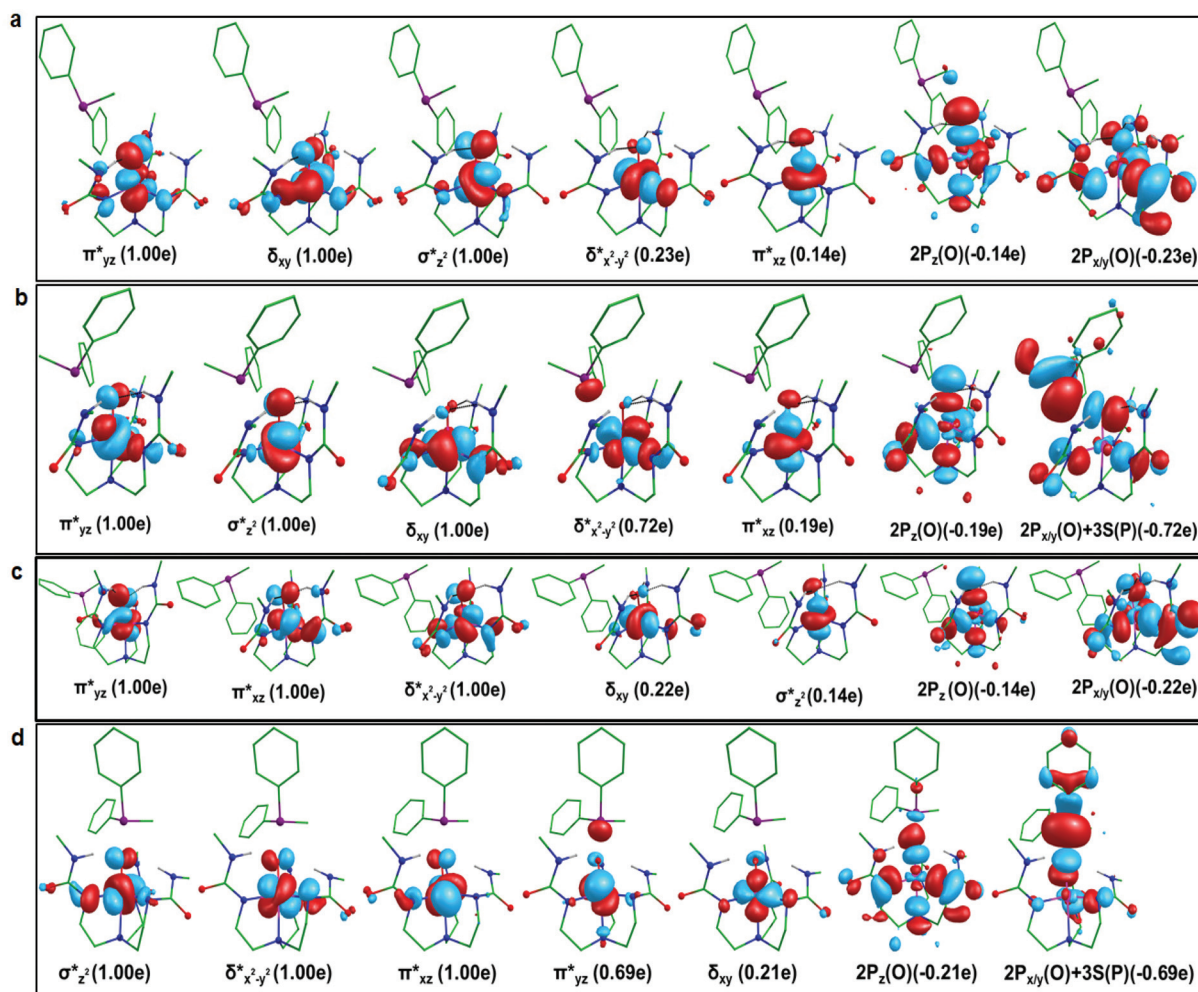
Fig. 7 Spin natural orbitals and their occupations in (a) $^4RC_{1(\sigma)}$, (b) $^4TS_{1(\delta)}$, (c) $^4RC_{1(\delta)}$, (d) $^4TS_{1(\sigma)}$. The negative occupation in φ signifies a β spin electron.

observation of lower yield for the PPhMe₂ compared to PPh₂Me.[14] The Mn–O–P angle is computed to be 117.59° along with the spin density of 3.616 on the Mn centre, leaving a significant amount of negative spins on the O and P centres in $^4TS_2$ (see Fig. 6b and g). Spin natural orbitals reveal that the computed pathway in PPhMe₂ (see Fig. S3 in the ESI†) is also the δ-pathway. The Mn–O bond is elongated by 0.01 Å than that in $^4TS_{1(\delta)}$, and the limiting O···P distance is also lengthened by 0.04 Å.

PPh₃ forms a very stable reactant complex ($^4RC_3$) with the catalyst [Mn^{IV}H₃buea(O)]⁻ which is exothermic by 43.4 kJ mol⁻¹ in the lowest-lying $S = 3/2$ spin state (see Fig. 2c). The formation of the reactant-complex in the other $S = 5/2$ ($^6RC_3$) and $S = 1/2$ ($^2RC_3$) states are also significantly exothermic compared to the free catalyst, but these states are lying 67.5 kJ mol⁻¹ and 90.8 kJ mol⁻¹ up-hill compared to that of $^4RC_3$ (see Fig. 2c). This extra stability of RC plays a crucial role in the reaction kinetics of this species. Compared to the other two substrates, PPh₂Me and PPhMe₂, the stability of the reactant complex species in the $S = 3/2$ spin state is ~2 times higher

making $^4RC_3$ comparatively reluctant to take part in the oxygen transfer mechanism. The intrinsic barrier ($^4RC_3 \rightarrow$ $^4TS_3$) for the OAT reaction with PPh₃ is estimated to be 63.3 kJ mol⁻¹ associated with the $S = 3/2$ surface (see Fig. 2c). This energy barrier is 20.0 kJ mol⁻¹ and 18.5 kJ mol⁻¹ higher than that of the PPh₂Me and PPhMe₂ substrates, respectively in the same surface. The DFT optimised structure of the transition state, $^4TS_3$, along with the spin density plot is shown in Fig. 6c and h. The Mn–O distance at $^4TS_3$ is elongated to 1.72 Å, and at the transition state, the O···P distance is calculated to be 2.40 Å. In the rate-limiting transition state, the spin density on the Mn centre is increased by 0.728 with the residual spins of −0.257 and −0.238 on the O and P centre, respectively (see Fig. 6c and h). The Mn–O–P angle of 120.61° suggests the δ pathway for the oxo-transfer which is manifested by the transfer of a significant amount of spin-up electron to the metal $\delta^*_{x^2-y^2}$ orbital from the phosphorus 3S and oxygen 2P orbitals, respectively (see Fig. S4 in the ESI†). Here only two H-bonds are found to be stronger while the third one is broken as PPh₃ approaches from this side. Similarly, the product formation
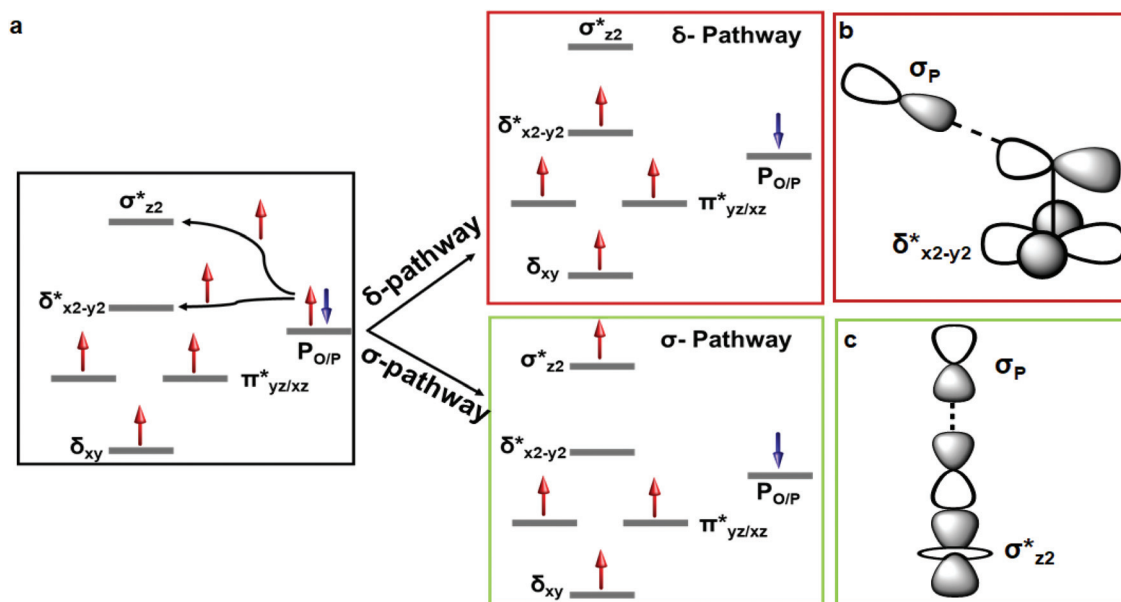
Fig. 8 (a) Electron-shift diagrams describing two alternative electronic reorganization modes between the metal-d and O/P orbitals in the $S = 3/2$ state during the oxygen atom transfer step from the catalyst $[Mn^{IV}H_3buea(O)]^-$ to the PPh_2Me, the δ-path(above one) and the σ-pathway (bottom one), (b) the predicted orbital interactions, which steer the orientation of $^4TS_{1(\delta)}$ and (c) the predicted orbital interactions, which steer the orientation of $^4TS_{1(\sigma)}$.

step is exothermic maintaining the two-state reactivity trend between the high-lying $S = 5/2$, and the low-lying $S = 3/2$ state and $^6P_3$ is stabilised by 207.3 kJ mol^{-1} as compared to the free catalyst. The DFT computed rate of the oxygen atom transfer reaction is calculated to be 58 M^{-1} s^{-1} which is $\sim 3 \times 10^3$ times lower than that of the most facile PPh_2Me. This DFT computed lower rate for the PPh_3 substrate is in accordance with the experiments where PPh_3 was found to be unreactive with the $[Mn^{IV}H_3buea(O)]^-$ catalyst.

For the PCy_3 substrate, the cluster RC_4 is of higher energy than the separate reactants and therefore, we can assume that there was no stable reactant complex formation here and we can ignore it for this species from the reaction kinetics. The intrinsic barrier for oxygen atom transfer ($^4RC_4 \rightarrow {}^4TS_4$) from the free catalyst and the substrate is estimated to be 65.5 kJ mol^{-1} in the quartet energy surface (see Fig. 2d). In the limiting step, the r(Mn–O) and r(O···P) are estimated to be 1.71 Å and 2.60 Å, respectively (see Fig. 6d). The Mn–O bond elongation is the smallest for PCy_3 as compared to the other substrates while the limiting value of the O···P bond is the highest among all indicating the fact that, the approach of bulky PCy_3 to the metal–oxo centre causes significant steric repulsion which results in the contraction of Mn–oxo unit towards the H-bonding cavity as well as to minimise the steric cost, PCy_3 attacks the oxo-centre from a larger distance. This is supported by the decrease in the H-bond length cavity to 2.07 Å in one side, which is distorted in all complexes (see Table S1†). The Mn–O–P angle in the $^4TS_4$ is found to be 118.5° with the spin densities on metal, O and P centres are 3.599, −0.274 and −0.314, respectively (see Fig. 6i). Here also in PCy_3, the α-electron is transferred to the metal $\delta^*_{x^2-y^2}$ orbital leading to

a δ-type pathway (see Fig. S5†). Here the formation of the product, $^6P_4$ is 150.9 kJ mol^{-1} exergonic than that of the free reactants in the ground state. The DFT calculated rate for the PCy_3 substrate is found to be 19.2 M^{-1} s^{-1}. Here, the low rate for the oxygen-transfer along with the lowest formation energy for the product, results in a lack of driving force for the reaction and this is in line with the experimental observation that PCy_3 does not react with the catalyst.

For PMe_3 the formation of the reactant complex is exothermic by 30.3 kJ mol^{-1} in the quartet surface followed by the oxo-transfer transition state, $^4TS_5$ associated with the intrinsic barrier of 63.5 kJ mol^{-1} in the $S = 3/2$ spin state (see Fig. S6 in the ESI†). The elongation of the Mn–O bond in $^4TS_5$ is found to be 1.72 Å which is comparable with the PPh_3. The respective spin densities on the Mn, O and P centres in the transition state are 3.598, −0.294, and −0.271 and the Mn–O–P angle is found to be 115.4° suggesting a δ-type pathway (see Fig. 6e, j and Fig. S7 in the ESI†). The distance between the O and the P centre in $^4TS_5$ is found to be 2.44 Å. The comparatively higher O···P distance in the limiting condition is similar to the case of $PPhMe_2$, i.e., with a decrease in the steric hindrance the substrate will come closer to the Mn–O moiety and get repulsed due to the destabilising electrostatic interaction from the dangling polar group of the buea. The calculated rate for the PMe_3 is 42.7 M^{-1} s^{-1}, which is quite low from a reaction perspective, and we can conclude that PMe_3 is not suitable enough for the oxygen atom transfer reaction by the Mn^{IV}=O catalyst.

Comparison between oxygen and sulphur atom transfer reaction

The structure and bonding of $[Mn^{IV}H_3buea(S)]^-$ species was discussed in the earlier section, and here we have attempted to

compute the transition states for the sulphur atom transfer (SAT) reaction by this species with PPh$_2$Me as the substrate. The SAT reactions are typical of metal ions such as V^{IV}, Mo^{IV} and Re^{IV} possessing terminal sulphido bridges and are common also in dinuclear Fe and Mn chemistry.[43–46,75] Our work has been motivated by a similar type of Fe^{III}=S species which is known to be involved in the sulphur atom transfer reactions.[46] The DFT computed potential energy surface diagram for the sulphur atom transfer (SAT) is depicted in Fig. 5. As we have discussed in the previous section, unlike the oxygen atom transfer, SAT involves both the $S = 5/2$ and $S = 3/2$ spin states in the reaction kinetics as the energy gap between these two states is marginal (8.6 kJ mol^{-1}). This gap decreases and becomes nearly degenerate when we consider reactant complex formation (energy gap of 0.1 kJ mol^{-1}). Upon careful investigation on the structures of the reactant complex, the Mn–S bond lengths in the $S = 5/2$ and $S = 3/2$ do not differ much, 2.34 Å and 2.33 Å, respectively (see Table S1†). Moreover, the spin density values of 3.907/0.763 and 4.034/−0.904 on the Mn/S centres in the ^{6}RC$_S$ and ^{4}RC$_S$ are indicating towards the existence of the Mn^{III}–S$^·$ species with spin-up and spin-down on the sulphido radical in the ^{6}RC$_S$ and ^{4}RC$_S$, respectively (see Table S6†). All our attempts to obtain the ^{6}TS$_S$ transition state collapsed to the product suggesting a flat potential energy surface with no/very small barrier height. To affirm the barrier height, we performed a relaxed potential energy surface scan along the S and P bond from 2.25 Å to 2.8 Å (see Fig. S8 in the ESI†) and this yielded a barrier height 0.4 kJ mol^{-1} (^{6}RC$_S$ → ^{6}TS$_S$), reflecting a barrierless reaction for the SAT on the sextet surface. The barrier height in the quartet surface is estimated to be 16.8 kJ mol^{-1} (^{4}RC$_S$ → ^{4}TS$_S$) (see Fig. 5). Minimal/no barriers for the SAT reaction compared to OAT suggest a very facile and fast transfer of sulphur compared to the OAT reaction, while there is no experimental proof for this observation, SAT reactions are found to be faster for Fe^{III}=S species compared to Fe^{IV}=O, suggesting a similar trend could be possible also in Mn systems. In the transition state, the r(Mn–S) is found to be 2.46 Å, and the distance between the P and the S centres is 2.70 Å (see Fig. 9). It is seen that the H-bond cavity around the metal centre is distorted in both in ^{6}TS$_S$ and ^{4}TS$_S$ (see Fig. S9 in the ESI†); as a result, the Mn–S bond is elongated and provides more room for the approach of the substrate PPh$_2$Me, making the S-transfer more facile. The enhanced spin density of 4.363 on Mn with the significant amount of residual spins of 0.266 and 0.216 on the S and P centres in ^{6}TS$_S$ reveals the fact that there is a considerable rearrangement of spins that take place during the transition (see Table S6† and Fig. 9). A β-spin electron from phosphorus has been transferred to the δ$_{xy}$ orbital of the Mn atom suggesting a different δ pathway being operational here compared to the Mn^{IV}=O species. As the Mn atoms already exist in the Mn^{III} state here, the low lying δ*$_{x^2−y^2}$ orbital is already occupied leaving only the σ*$_{z^2}$ orbital empty. As the σ*$_{z^2}$ is strongly destabilised, reaction channels prefer a β-electron transfer to the δ$_{xy}$ orbital. However, this is expected to reduce the EER
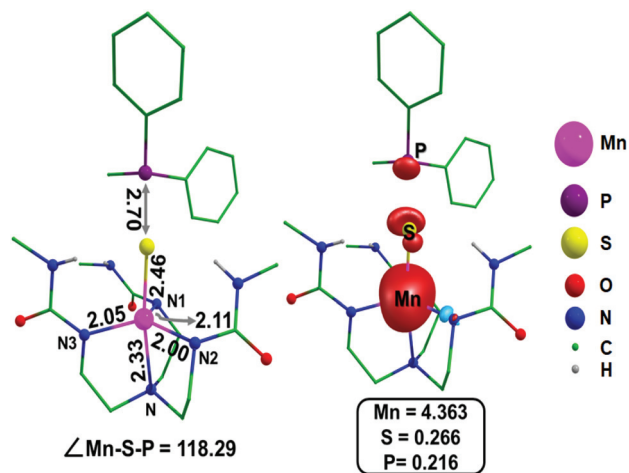

Fig. 9 DFT/B3LYP-D3 optimised structures and spin density plot of ^{6}TS$_S$ species.

at the transition state, suggesting strong orbital control reactivity.

Comparative reactivity pattern among the PR$_3$ substrates

In this section, we have concentrated on the comparisons across the substrates, and we have explored the reasons for the variation in the computed barrier heights. For all substrates, the $S = 5/2$ state is found to be higher in energy, suggesting OAT to be taking place *via* the $S = 3/2$ surface. The OAT reactions are two-electron reduction process and occur at one step.

As per the computed barrier heights at the $S = 3/2$ state, calculations predict the following reactivity pattern PCy$_3$ < PMe$_3$ < PPh$_3$ < PPhMe$_2$ < PPh$_2$Me. To understand the origin of the difference in the barrier, EDA analysis was performed which reveal that the trend in the barrier heights is correlated to the computed electronic interaction energy (E_{int}), orbital interaction energy (E_{orb}), and steric energy (E_{steric}) between the two fragments PR$_3$ and [Mn^{IV}H$_3$buea(O/S)]$^-$ species (see Table S7 in the ESI† and Fig. 10 in the main manuscript). The steric repulsive energies between two reacting species follow the trend PPh$_2$Me > PPhMe$_2$ > PPh$_3$ > PCy$_3$ > PMe$_3$ while the trend in the electronic interaction energies is as PPh$_2$Me > PCy$_3$ > PPh$_3$ > PPhMe$_2$ > PMe$_3$. Moreover, the orbital interaction energy decreases as PPhMe$_2$ > PPh$_2$Me > PPh$_3$ > PCy$_3$ > PMe$_3$. The first contribution is surely the destabilising one, and the next two are the stabilising contributions to the estimated transition state energies. For PPh$_2$Me substrate, the energy penalty due to the highest steric repulsion is more than compensated by the energy gain due to stabilising electronic interaction and orbital interaction energies, making it the most reactive among all substrates. On the other hand, although steric energy for PPh$_3$ is not the highest, the lower amount of orbital energy makes this substrate less reactive. Similarly, the lower reactivity of PMe$_3$ is explained by the lowest orbital as well as the electronic interaction energies (see Table S7 in the ESI† and Fig. 10 in the main manuscript). Furthermore, at the
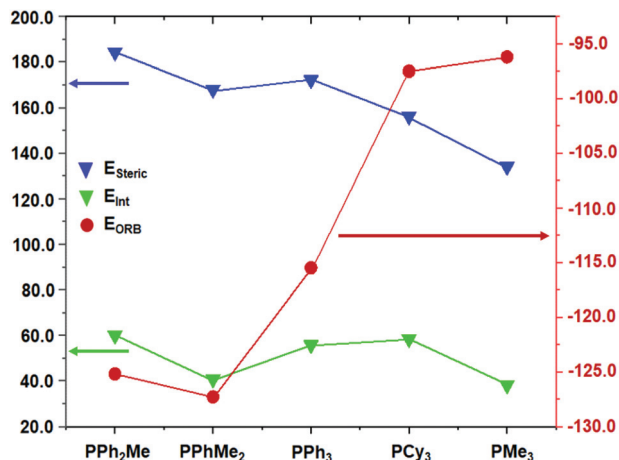
Fig. 10 Correlation between the dependence of energy barrier on the steric energy, electronic and orbital interaction energies (all in kJ mol^{-1}) of the transition states for different substrates. The left Y-axis values correspond to the steric energies (blue, positive Y-axis values) and electronic interaction energies (green, negative Y-axis values) and the right Y-axis values are for orbital energies (red).

quartet transition state, transfer of one electron from the substrate to the catalyst leaves a radical character at the substrate and substrates which can stabilise this radical character are likely to yield a lower barrier. At this front, both PMe$_3$ and PCy$_3$ having aliphatic substitutions at the phosphorous atom offer very little delocalisation and hence add significant barrier heights with PCy$_3$ being weaker than PMe$_3$. While PPh$_3$ with three phenyl groups has the lowest radical character at the phosphorous atom (see Fig. 6f–j), it is expected to stabilise the radical character but suffer from significant strain in

approaching the oxygen due to its bulkiness. The PPh$_2$Me substrate thus offers the best balance between these two ends, stabilising the radical character with two available phenyl groups and the presence of one methyl offers a closer approach to oxygen making it the most reactive among all. The PCy$_3$ turns out to be the worst as it neither provides delocalisation of the radical present at the phosphorous atom (the largest radical character at the P atom, see Fig. 6i) nor ease the sterics (the longest P⋯O distance) to enable a strong overlap between the P and O atoms. While the difference in estimated barrier heights between PPh$_2$Me and PPhMe$_2$ is marginal, the smaller barrier for PPh$_2$Me reveals that stabilisation of the radical plays a vital role compared to the sterics, suggesting a delicate balance between various factors that are played in controlling the reactivity with different substrates.

To further understand the nature of transition states with respect to various substrates, we have calculated the bond make-break average at the transition state with respect to the reactant and the product. While this has been utilised earlier for several organic reactions, there are only a few examples of such analysis for transition metals.[70] We have plotted the BFC$_{ava}$ with the corresponding transition state barrier computed for all species in Fig. 11. As the BFC$_{ava}$ represents the reaction coordinate, this is taken in the x-axis while the y-axis represents the corresponding barrier height. A larger BFC$_{ava}$ indicates that the transition state is a product-like while a smaller value indicates a reactant-like transition state. From Fig. 11, it is clear that PCy$_3$ is least reactive as it possesses a very early transition state compared to all (BFC$_{ava}$ is 21.7), while the PPh$_2$Me is most reactive as its transition states are product-like (BFC$_{ava}$ is 30.5 for ^{4}TS$_{1(\delta)}$ and 35.8 for ^{4}TS$_{1(\sigma)}$). The trend observed in the reactivity pattern is well reflected in the
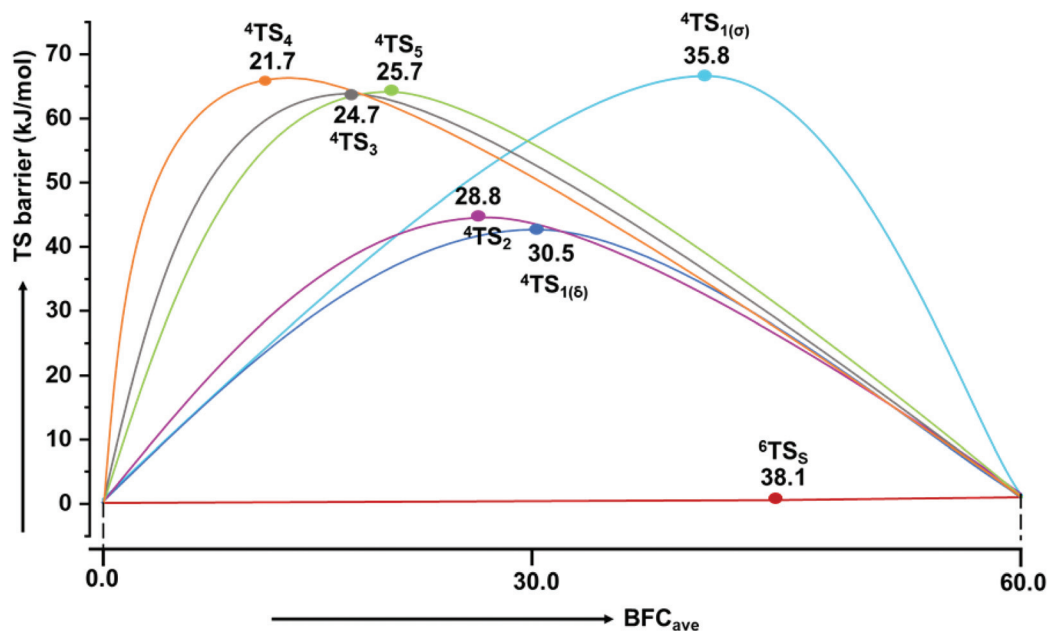
Fig. 11 B3LYP-D3 computed energy profile of TS barrier vs. BFC$_{ave}$ for the oxygen (with PPh$_2$Me, PPhMe$_2$, PPh$_3$, PCy$_3$, PMe$_3$ substrates) and sulphur (with PPh$_2$Me substrate) atom transfer reactions using [Mn^{IV}H$_3$buea(O)]$^-$ as well as [Mn^{IV}H$_3$buea(S)]$^-$ catalyst.

computed BFC_{ava}, offering a potential tool to predict reactivity based on this analysis (Table S8 in the ESI†). A late transition state is found with the PPh$_2$Me substrate when reacting with the [Mn^{IV}H$_3$buea(S)]$^-$ catalyst (see Fig. 11).

Conclusions

Here using a combination of *ab initio* CASSCF/NEVPT2 and DFT calculations, we have explored the mechanism of OAT by [Mn^{IV}H$_3$buea(O)]$^-$ and its congener [Mn^{IV}H$_3$buea(S)]$^-$. The conclusions derived from this work are highlighted below,

(i) The detailed *ab initio* multi-reference CASSCF/NEVPT2 calculations reveal that the ground $S = 3/2$ state is strongly admixed with several low-lying quartets. Particularly the $\delta_{xy}^{1}\pi^{\star}_{yz}^{1}\pi^{\star}_{xz}^{1}\delta^{\star}_{x^2-y^2}^{0}\sigma^{\star}_{z^2}^{0}$ configuration was found to mix strongly with the other two triplets, namely $\delta_{xy}^{1}\pi^{\star}_{yz}^{1}\pi^{\star}_{xz}^{1}\delta^{\star}_{x^2-y^2}^{0}\sigma^{\star}_{z^2}^{1}$ and $\delta_{xy}^{1}\pi^{\star}_{yz}^{1}\pi^{\star}_{xz}^{0}\delta^{\star}_{x^2-y^2}^{1}\sigma^{\star}_{z^2}^{0}$ configurations. This admixing of wavefunction was found to alter upon the approach of the substrate, *i.e.* at the reactant complex when the substrate attached to the catalyst by dispersive forces, the $\delta_{xy}^{1}\pi^{\star}_{yz}^{1}\pi^{\star}_{xz}^{0}\delta^{\star}_{x^2-y^2}^{0}\sigma^{\star}_{z^2}^{1}$ configuration dominates the ground state triplet. While a traditional two-state reactivity was unfounded here, a strong multi-reference character of the ground state quartet suggests multistate reactivity scenario involving various triplet states.

(ii) The OAT reaction with PPh$_2$Me, PPhMe$_2$, PCy$_3$, PPh$_3$, and PMe$_3$ substrates was performed, and the barrier height at $S = 3/2$ surface was found to decrease in the following order PCy$_3$ > PMe$_3$ > PPh$_3$ > PPhMe$_2$ > PPh$_2$Me and this was consistent with the experimental observations. In all cases, a dominant spin-up electron transfer from the substrate to the metal $\delta^{\star}_{x^2-y^2}$ orbital is noted at the transition state suggesting a low-energy δ-type pathway. While this is unusual, a strong multireference character of the ground state with significant oxyl radial character at the $\delta^{\star}_{x^2-y^2}$ orbital facilitates such a transfer.

(iii) Mechanism of SAT with the [Mn^{IV}H$_3$buea(S)]$^-$ catalyst using PPh$_2$Me species is predicted, and this species is found to react *via* the β-electron transfer path and is thus expected to respond faster than the corresponding Mn^{IV}=O species.

To this end, here we have proposed for the first time, intricate electron transfer paths in OAT reactions and how this contributes to the reactivity of the Mn^{IV}=O species and the mechanism and the concepts established here have scope beyond the examples studied.

Conflicts of interest

There are no conflicts to declare.

Acknowledgements

References

1 L. K. Woo, *Chem. Rev.*, 1993, **93**, 1125–1136.

2 V. K. Yachandra, K. Sauer and M. P. Klein, *Chem. Rev.*, 1996, **96**, 2927–2950.

3 R. Friemann, M. M. Ivkovic-Jensen, D. J. Lessner, C.-L. Yu, D. T. Gibson, R. E. Parales, H. Eklund and S. Ramaswamy, *J. Mol. Biol.*, 2005, **348**, 1139–1151.

4 B. A. Diner, D. A. Force, D. W. Randall and R. D. Britt, *Biochemistry*, 1998, **37**, 17931–17943.

5 B. S. Lane and K. Burgess, *Chem. Rev.*, 2003, **103**, 2457–2474.

6 R. J. Nick, G. B. Ray, K. M. Fish, T. G. Spiro and J. T. Groves, *J. Am. Chem. Soc.*, 1991, **113**, 1838–1840.

7 V. L. Pecoraro, M. J. Baldwin and A. Gelasco, *Chem. Rev.*, 1994, **94**, 807–826.

8 B. Lassalle-Kaiser, C. Hureau, D. A. Pantazis, Y. Pushkar, R. Guillot, V. K. Yachandra, J. Yano, F. Neese and E. Anxolabéhère-Mallart, *Energy Environ. Sci.*, 2010, **3**, 924–938.

9 R. D. Britt, K. A. Campbell, J. M. Peloquin, M. L. Gilchrist, C. P. Aznar, M. M. Dicus, J. Robblee and J. Messinger, *Biochim. Biophys. Acta, Bioenerg.*, 2004, **1655**, 158–171.

10 R. H. Holm, *Chem. Rev.*, 1987, **87**, 1401–1449.

11 J. P. T. Zaragoza, R. A. Baglia, M. A. Siegler and D. P. Goldberg, *J. Am. Chem. Soc.*, 2015, **137**, 6531–6540.

12 A. A. Massie, M. C. Denler, R. Singh, A. Sinha, E. Nordlander and T. A. Jackson, *Chem. – Eur. J.*, 2020, **26**, 900–912.

13 M. C. Denler, A. A. Massie, R. Singh, E. Stewart-Jones, A. Sinha, V. W. Day, E. Nordlander and T. A. Jackson, *Dalton Trans.*, 2019, **48**, 5007–5021.

14 T. H. Parsell, R. K. Behan, M. T. Green, M. P. Hendrich and A. S. Borovik, *J. Am. Chem. Soc.*, 2006, **128**, 8728–8729.

15 Y.-M. Lee, M. Yoo, H. Yoon, X.-X. Li, W. Nam and S. Fukuzumi, *Chem. Commun.*, 2017, **53**, 9352–9355.

16 B. W. Kail, L. M. Pérez, S. D. Zarić, A. J. Millar, C. G. Young, M. B. Hall and P. Basu, *Chem. – Eur. J.*, 2006, **12**, 7501–7509.

17 H. Hirao, L. Que Jr., W. Nam and S. Shaik, *Chem. – Eur. J.*, 2008, **14**, 1740–1756.

18 G. Mukherjee, C. W. Z. Lee, S. S. Nag, A. Alili, F. G. C. Reinhard, D. Kumar, C. V. Sastri and S. P. de Visser, *Dalton Trans.*, 2018, **47**, 14945–14957.

19 R. Gupta, T. Taguchi, B. Lassalle-Kaiser, E. L. Bominaar, J. Yano, M. P. Hendrich and A. S. Borovik, *Proc. Natl. Acad. Sci. U. S. A.*, 2015, **112**, 5319–5324.

20 Y. Kono and I. Fridovich, *J. Biol. Chem.*, 1983, **258**, 6015–6019.

21 R. J. Nick, G. B. Ray, K. M. Fish, T. G. Spiro and J. T. Groves, *J. Am. Chem. Soc.*, 1991, **113**, 1838–1840.

22 A. A. Massie, M. C. Denler, L. T. Cardoso, A. N. Walker, M. K. Hossain, V. W. Day, E. Nordlander and T. A. Jackson, *Angew. Chem., Int. Ed.*, 2017, **56**, 4178–4182.

23 D. B. Rice, A. A. Massie and T. A. Jackson, *Inorg. Chem.*, 2019, **58**, 13902–13916.

24 Y.-M. Lee, S. Kim, K. Ohkubo, K.-H. Kim, W. Nam and S. Fukuzumi, *J. Am. Chem. Soc.*, 2019, **141**, 2614–2622.

25 X.-X. Li, M. Guo, B. Qiu, K.-B. Cho, W. Sun and W. Nam, *Inorg. Chem.*, 2019, **58**, 14842–14852.

26 N. Sharma, J. Jung, K. Ohkubo, Y.-M. Lee, M. E. El-Khouly, W. Nam and S. Fukuzumi, *J. Am. Chem. Soc.*, 2018, **140**, 8405–8409.

27 S. Biswas, A. Mitra, S. Banerjee, R. Singh, A. Das, T. K. Paine, P. Bandyopadhyay, S. Paul and A. N. Biswas, *Inorg. Chem.*, 2019, **58**, 9713–9722.

28 V. F. Oswald, A. C. Weitz, S. Biswas, J. W. Ziller, M. P. Hendrich and A. S. Borovik, *Inorg. Chem.*, 2018, **57**, 13341–13350.

29 S. K. Barman, J. R. Jones, C. Sun, E. A. Hill, J. W. Ziller and A. S. Borovik, *J. Am. Chem. Soc.*, 2019, **141**, 11142–11150.

30 C. E. MacBeth, R. Gupta, K. R. Mitchell-Koch, V. G. Young, G. H. Lushington, W. H. Thompson, M. P. Hendrich and A. S. Borovik, *J. Am. Chem. Soc.*, 2004, **126**, 2556–2567.

31 R. Gupta, C. E. MacBeth, V. G. Young and A. S. Borovik, *J. Am. Chem. Soc.*, 2002, **124**, 1136–1137.

32 T. H. Parsell, M.-Y. Yang and A. S. Borovik, *J. Am. Chem. Soc.*, 2009, **131**, 2762–2763.

33 R. Gupta and A. S. Borovik, *J. Am. Chem. Soc.*, 2003, **125**, 13234–13242.

34 D. F. Leto, A. A. Massie, D. B. Rice and T. A. Jackson, *J. Am. Chem. Soc.*, 2016, **138**, 15413–15424.

35 K.-B. Cho, S. Shaik and W. Nam, *J. Phys. Chem. Lett.*, 2012, **3**, 2851–2856.

36 A. Sen, N. Vyas, B. Pandey, M. Jaccob and G. Rajaraman, *Isr. J. Chem.*, DOI: 10.1002/ijch.201900142.

37 S. P. de Visser, Y.-M. Lee and W. Nam, *Eur. J. Inorg. Chem.*, 2008, **2008**, 1027–1030.

38 M. Retegan, V. Krewald, F. Mamedov, F. Neese, W. Lubitz, N. Cox and D. A. Pantazis, *Chem. Sci.*, 2016, **7**, 72–84.

39 A. Ansari and G. Rajaraman, *Dataset Pap. Sci.*, 2014, **2014**, 753131.

40 S. P. de Visser, M. G. Quesne, B. Martin, P. Comba and U. Ryde, *Chem. Commun.*, 2014, **50**, 262–282.

41 M. Jaccob, A. Ansari, B. Pandey and G. Rajaraman, *Dalton Trans.*, 2013, **42**, 16518–16526.

42 D. Usharani, D. C. Lacy, A. S. Borovik and S. Shaik, *J. Am. Chem. Soc.*, 2013, **135**, 17090–17104.

43 J. P. Donahue, *Chem. Rev.*, 2006, **106**, 4747–4783.

44 T. D. Ju, R. F. Lang, G. C. Roper and C. D. Hoff, *J. Am. Chem. Soc.*, 1996, **118**, 5328–5329.

45 J.-J. Wang, O. P. Kryatova, E. V. Rybak-Akimova and R. H. Holm, *Inorg. Chem.*, 2004, **43**, 8092–8101.

46 A. Dey, R. K. Hocking, P. Larsen, A. S. Borovik, K. O. Hodgson, B. Hedman and E. I. Solomon, *J. Am. Chem. Soc.*, 2006, **128**, 9825–9833.

47 M. J. Frisch, G. W. Trucks, H. B. Schlegel, G. E. Scuseria, M. A. Robb, J. R. Cheeseman, G. Scalmani, V. Barone,

B. Mennucci and G. A. Petersson, *R. A. Gaussian 09, Inc.*, Wallingford CT, 2009, vol. 121, pp. 150–166.

48 M. J. Frisch, G. W. Trucks, H. B. Schlegel, G. E. Scuseria, M. A. Robb, J. R. Cheeseman, G. Scalmani, V. Barone, B. Mennucci and G. A. Petersson, *Gaussian 09, Revision d. 01*, Gaussian, Wallingford, 2009.

49 A. D. Becke, *J. Chem. Phys.*, 1997, **107**, 8554–8560.

50 A. D. Becke, *J. Chem. Phys.*, 1993, **98**, 5648–5652.

51 A. D. Becke, *Phys. Rev. A*, 1988, **38**, 3098–3100.

52 W. R. Wadt and P. J. Hay, *J. Chem. Phys.*, 1985, **82**, 284–298.

53 P. J. Hay and W. R. Wadt, *J. Chem. Phys.*, 1985, **82**, 270–283.

54 W. J. Hehre, R. Ditchfield and J. A. Pople, *J. Chem. Phys.*, 1972, **56**, 2257–2261.

55 A. V. Marenich, C. J. Cramer and D. G. Truhlar, *J. Phys. Chem. B*, 2009, **113**, 6378–6396.

56 S. Grimme, J. Antony, S. Ehrlich and H. Krieg, *J. Chem. Phys.*, 2010, **132**, 154104.

57 S. Grimme, S. Ehrlich and L. Goerigk, *J. Comput. Chem.*, 2011, **32**, 1456–1465.

58 F. Martin and H. Zipse, *J. Comput. Chem.*, 2005, **26**, 97–105.

59 F. Neese, The ORCA program system, *Wiley Interdiscip. Rev.: Comput. Mol. Sci.*, 2012, **2**, 73–78.

60 C. van Wüllen, *J. Chem. Phys.*, 1998, **109**, 392–399.

61 E. van Lenthe, E. J. Baerends and J. G. Snijders, *J. Chem. Phys.*, 1993, **99**, 4597–4610.

62 D. Ganyushin and F. Neese, *J. Chem. Phys.*, 2006, **125**, 24103.

63 S. I. Gorelsky, 2011, *AOMIX*, Department of Chemistry, York University, Toronto, ON.

64 G. A. Zhurko, 2014, *ChemCraft software, version 1.6*.

65 R. L. Halbach, D. Gygi, E. D. Bloch, B. L. Anderson and D. G. Nocera, *Chem. Sci.*, 2018, **9**, 4524–4528.

66 X. Wu, M. S. Seo, K. M. Davis, Y.-M. Lee, J. Chen, K.-B. Cho, Y. N. Pushkar and W. Nam, *J. Am. Chem. Soc.*, 2011, **133**, 20088–20091.

67 J. M. Charnock, C. D. Garner, A. X. Trautwein, E. Bill, H. Winkler, K. Ayougou, D. Mandon and R. Weiss, *Angew. Chem., Int. Ed. Engl.*, 1995, **34**, 343–346.

68 R. L. Shook and A. S. Borovik, *Chem. Commun.*, 2008, 6095–6107.

69 K. Kavitha and P. Venuvanalingam, *J. Chem. Soc., Perkin Trans. 2*, 2002, 2130–2139.

70 R. Jagadeesan, G. Sabapathi, J. Madhavan and P. Venuvanalingam, *Inorg. Chem.*, 2018, **57**, 6833–6846.

71 N. Y. Lee, D. Mandal, S. H. Bae, M. S. Seo, Y.-M. Lee, S. Shaik, K.-B. Cho and W. Nam, *Chem. Sci.*, 2017, **8**, 5460–5467.

72 K. A. Prokop, S. P. de Visser and D. P. Goldberg, *Angew. Chem., Int. Ed.*, 2010, **49**, 5091–5095.

73 B. Helmich-Paris, *J. Chem. Phys.*, 2019, **150**, 174121.

74 P. Comba, D. Faltermeier, S. Krieg, B. Martin and G. Rajaraman, *Dalton Trans.*, 2020, **49**, 2888–2894.

75 M. Surducan, D. Lup, A. Lupan, S. V. Makarov and R. Silaghi-Dumitrescu, *J. Inorg. Biochem.*, 2013, **118**, 13–20.